A Comparison of Roll and Nonroll Convection and the Subsequent Deepening Moist Convection: An LEM Case Study Based on SCMS Data

QIAN HUANG

College of Atmospheric Sciences, Lanzhou University, Lanzhou, China

JOHN H. MARSHAM AND DOUGLAS J. PARKER

Institute for Atmospheric Science, The School of the Environment, University of Leeds, Leeds, United Kingdom

WENSHOU TIAN

College of Atmospheric Sciences, Lanzhou University, Lanzhou, China

TAMMY WECKWERTH

Earth Observing Laboratory, National Center for Atmospheric Research, Boulder, Colorado

(Manuscript received 6 November 2007, in final form 10 June 2008)

ABSTRACT

Rolls observed during the Small Cumulus Microphysical Study (SCMS) field campaign are simulated using a large eddy model (LEM). The simulated boundary layer properties were in a good agreement with sounding profiles and aircraft observations, and the observed boundary layer rolls were reproduced by the model. Rolls started to decay when $-Z_i/L$ exceeded a threshold, with a value between 5 and 45. Here Z_i and L refer to the height of the top of convective boundary layer and the Monin–Obukhov length, respectively. This value was found to depend on a nondimensional combination of the low-level wind shear, the height of the CBL, and the eddy velocity scale. Larger surface buoyancy fluxes and smaller shears gave higher thresholds. For the case modeled, rolls persisted for surface buoyancy fluxes less than 110 W m^{-2}, and formed for boundary layer wind shears greater than 5×10^{-3} s^{-1}, which is consistent with previous studies.

The simulated roll convection was compared with a nonroll simulation, which was identical except for the wind and the wind shear used. In both the roll and nonroll cases the variability in convective inhibition (CIN) was dominated by the variability in the source air, rather than the lifting of the top of the boundary layer by the convection. Stronger moist updrafts existed in the nonroll convection, whereas roll convection gave a more symmetrical distribution of up and downdrafts, with stronger downdrafts than the nonroll case. The nonroll convection simulations have lower minimum values of CIN and clouds develop 15 min earlier in this case.

1. Introduction

The advent of high-resolution (grid spacing $\simeq$1 km) nonhydrostatic numerical weather prediction (NWP) models has led to a resurgence of interest in attempting to improve forecasts of the initiation of deep convection. Such NWP models do not resolve boundary layer processes, but can resolve large deep convective systems. Recent field campaigns have also addressed the processes involved in the initiation of convection, in particular, the International H_2O Project 2002 (IHOP_2002), which took place at the southern Great Plains of the United States, the Convective Storm Initiation Project (CSIP) conducted in the southern United Kingdom and the Convective and Orographically induced Precipitation Study (COPS), which took place in the Black Forest region of southern Germany and eastern France. Convective storms originated from the boundary layer in 94% of cases from CSIP (Browning et al. 2007), and in at least 50% of cases from

Corresponding author address: Qian Huang, College of Atmospheric Sciences, Lanzhou University, Lanzhou 730000, China.
E-mail: qianhuang@lzu.edu.cn

DOI: 10.1175/2008MWR2450.1

IHOP_2002 (Wilson and Roberts 2006). In such cases, storms are initiated when warm moist updrafts from the boundary layer can overcome the convective inhibition (CIN) and allow deeper moist convection to develop.

Boundary layer convection can take a variety of forms. Convective rolls have been shown to be common in the boundary layer and there is a substantial literature about them (Etling and Brown 1993). The initiation of deep convection is often controlled by mesoscale zones of convergence (e.g., Wilson and Schreiber 1986; Bennett et al. 2006; Wilson and Roberts 2006). However, when such mesoscale forcings are weak the variability within the boundary layer can provide a significant control on convective initiation and storms can be initiated from boundary layer circulations, such as boundary layer rolls (Weckwerth 2000). Where mesoscale forcings are stronger, the intersections of mesoscale convergence lines and rolls have also been observed to provide preferred locations for the initiation of convection (e.g., Wilson et al. 1992; Crook et al. 1991; Atkins et al. 1998; Xue and Martin 2006). It has been noted that the variability induced by boundary layer rolls can make single radio soundings unrepresentative of the boundary layer air that contributes to storms, and this can significantly affect the local lifting condensation level, convective available potential energy (CAPE), and CIN (e.g., Weckwerth 1996; Crook 1996). The importance of rolls for the initiation of deep convection is, however, much less well explored than the factors controlling roll formation (Xue and Martin 2006).

In the past, many two-dimensional simulations were used to research the organization of convective rolls in the boundary layer (e.g., Mason and Sykes 1982; Marson 1985; Chlond 1987; Raasch 1990; Sykes et al. 1990). In these two-dimensional models it was assumed that the roll vortices were homogeneous along the roll axis. More recent studies have, however, shown the importance of using three-dimensional simulations (e.g., Mason and Thomson 1987; Sykes et al. 1990; Cuijpers and Duynkerke 1993; Moeng and Sullivan 1994; Glendening 1996; Xue and Martin 2006).

In this paper we use the Met Office large eddy model (LEM) to explicitly resolve boundary layer rolls observed on one day (14 August 1995) during the Small Cumulus Microphysical Study (SCMS) field campaign (Weckwerth et al. 1999). Although deep convective storms did not form on this particular day, there were both CAPE (940 J kg^{-1} at 0818 LT) and CIN (43 J kg^{-1} at 0818 LT), allowing a transition from boundary layer cumulus to deeper moist convection. Boundary layer convection with and without rolls is compared, in order to examine the potential significance of boundary layer rolls for the initiation of deep convection. Section 2 discusses the observations and the control simulation and section 3 investigates the factors determining the onset and breakdown of the rolls. Section 4 investigates how boundary layer rolls affect CIN and thus the deepening of the modeled moist convection.

2. Evaluation of the control simulation with observational data

a. *The observational case*

The SCMS field campaign took place in 1995 in Florida. This paper uses SCMS data from 14 August 1995. The SCMS data provides aircraft observations of boundary layer rolls [from the University of Wyoming King Air (UWKA) research aircraft] and surface based observations, as well as radiosonde profiles. More detailed discussions about this observational case can be found in Weckwerth et al. (1999), so only a brief outline is provided here.

Radar data from 14 August 1995 showed that the first mode of organized boundary layer convection was rolls (Weckwerth et al. 1999). The earliest linear features appeared at 0940 local time (LT; LT = UTC − 4 h). By 1025 LT these had developed into well-defined two-dimensional roll convection, with a spacing of approximately 1 km and aligned close to the surface wind. This spacing had increased to 1.5 km by 1126 LT, and by 1316 LT the rolls had become less organized. The boundary layer developed from a 200-m stable layer at 0819 LT to a convective layer later. The depth of the convective boundary layer (CBL) grew from 700 m at 1050 LT to 800 m at 1120 LT, and 1.3 km at 1310 LT. UWKA aircraft observations (Weckwerth et al. 1999) showed moist roll updrafts and dry roll downdrafts.

b. *LEM setup and initialization*

Three-dimensional simulations from version 2.3 of the Met Office LEM (Gray and Petch 2001) are used throughout this study. The LEM is a nonhydrostatic model, which can be run in one, two, or three dimensions. The equation set is Boussinesq and in this study the incompressible Boussinesq formulation was used, which uses a reference density that is constant with height. The model uses a Kessler rain scheme (only cloud water and rain were included, since ice processes were not important for the clouds studied). The domain size was 10 km × 10 km × 5 km with a horizontal grid spacing of 250 m (the sensitivities to grid spacings, and evidence supporting the use of a 250-m grid spacing are shown in section 2d). A vertically stretched grid was used with the minimum spacing of 1.5 m in the lowest

model level increasing to a maximum of 200 m above 2 km. The small vertical spacings in the surface layer enabled the calculation of near-surface fluxes of virtual potential temperature and momentum. Changing these smallest vertical grid spacings to 27 m did not, however, have significant effects on the model results (not shown). Periodic lateral boundary conditions were applied, with a rigid lid at the top of the model domain. To reduce the reflection of internal gravity waves, a Newtonian damping layer was applied above 3500 m.

The model control experiment (C1) was initialized with a radiosonde profile from 0818 LT and time-dependent surface fluxes, observed using the Flux-Portable Automated Mesonet (PAM) array at station PAM 3 (Weckwerth et al. 1999), were applied for 5 h. Initially, random perturbations (of ±0.01 K and 0.025 g kg^{-1}) were applied below 1000 m to allow convection to develop in the model. The time series of modeled kinetic energy indicated that this convection had "spun up" by 0950 LT. To account for the effects of unrepresented large-scale forcings, the modeled horizontally averaged potential temperature, water vapor mixing ratio (Q), and wind were relaxed to those observed by radiosondes, with a time scale of 2.5 h (e.g., Couvreux et al. 2005; Marsham et al. 2006). The surface geostrophic wind was calculated from the National Centers for Environmental Prediction–National Center for Atmospheric Research (NCEP–NCAR) 2.5° reanalysis. Geostrophic wind shear was calculated using the observed wind at 1000 m (from the radiosondes) and the NCEP–NCAR surface geostrophic wind (positive u is east and positive v is north). A series of simulations were then performed with different idealized geostrophic wind shears varying about this value (all with the geostrophic shear constant with height). A run with a geostrophic wind shear 2.5 times that calculated from the NCEP–NCAR reanalysis and the radiosondes was found to give rolls similar to observed and this is referred to as the control run (C1; Fig. 1). This control run was then used for a series of sensitivity studies, including the sensitivity to shear (section 3). A further sensitivity study, using a constant geostrophic wind above the top of the boundary layer (not shown), gave very similar boundary layer convection to that in the control run. This shows that idealizing the geostrophic wind profile to a constant shear did not significantly affect the results.

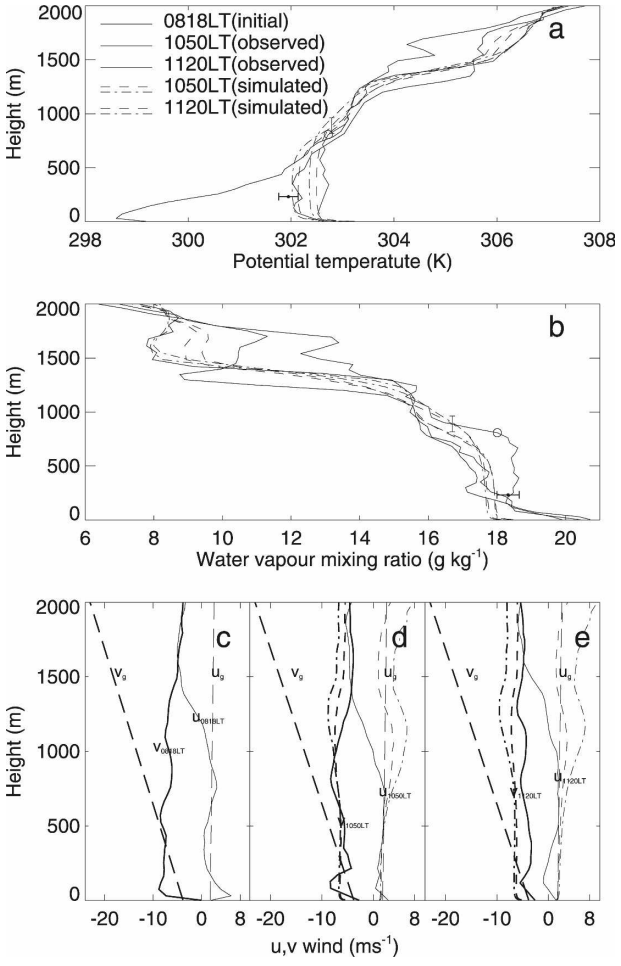

FIG. 1. Simulated and radiosonde profiles of (a) the potential temperature and (b) the water vapor mixing ratio, both at 0818, 1050, and 1120 LT. Dashed lines show results from C1; dash–dotted lines show results from the run without additional forcings (C1NOF). The modeled standard deviation in the height of convective boundary layer (Z_i) at 1120 LT is indicated by the solid bar. The black circle presents the CBL height from the radiosound at 1120 LT. Black dots and the thick solid bars present the mean and standard deviation of the aircraft data, which is from 232 m for 5 min around 1120 LT. (c), (d), (e) Simulated and observed winds at 0818, 1050, and 1120, respectively. The u winds are from the west and the v winds are from the south. Dashed lines show the standard run and dash–dotted lines the unforced run. Geostrophic winds from the model are also shown (ug and vg, long-dashed line).

c. The control simulation

Figure 1 shows mean model and radiosonde profiles. Within the boundary layer, the modeled potential temperature (θ) and Q profiles are within 0.5 K or 1.5 g kg^{-1} of those observed, which at the height of the aircraft flight track is within the variability shown by the aircraft data. The model profiles are smoother than those from the radiosondes, since the model profiles are mean profiles, while the radiosondes are affected by variability within the boundary layer. The simulated inversion (Z_i, the top of CBL) is at a higher altitude than the radio sounding. But the inversion height is within the simulated variability at 1120 LT, which is

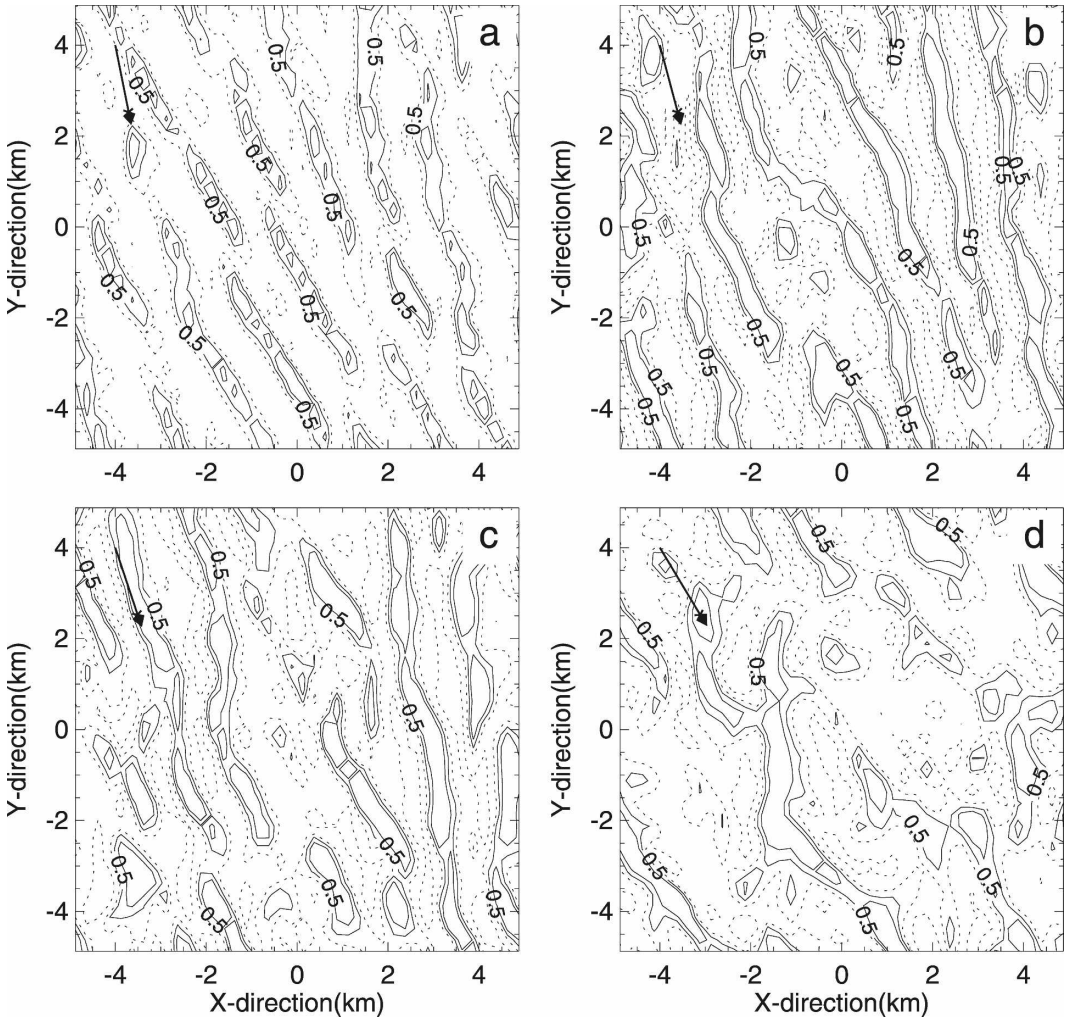

FIG. 2. The instantaneous vertical velocity fields at 237 m AGL at (a) 1018, (b) 1050, (c) 1100, and (d) 1220 LT of run C1. Contours are at ±0.5 and ±1.0 m s^{-1}. The mean CBL wind directions are represented by the arrows.

shown by the solid bar in Figs. 1a,b. Here we use the same criterion to compare the CBL height between the model horizontal mean and radio sounding profiles. The CBL height was determined by the maximum of the absolute value of the vertical moisture gradient ($\partial Q/\partial z$) (e.g., Wulfmeyer 1999; Couvreux et al. 2005) for both the radio sounding and the model. Although the simulated CBL height is at a higher altitude than that from the radio sounding, it is within the simulated variability at 1120 LT, which is shown by the solid bar in Figs. 1a,b. Above the CBL, there is a residual layer, which at 1120 LT reaches up to 1.2 km in the simulation, and 1.5 km for the radio sounding. A comparison of the forced (C1) and unforced (C1NOF, no relaxation) model runs (Fig. 1) shows that the relaxation toward the observed profiles has little effect within the boundary layer (similar to Couvreux et al. 2005). Differences between C1 and C1NOF are more significant above 1500 m, since there are larger differences between the model and the observations there.

At 1018 LT, the organized convective rolls are evident in the model (Fig. 2a), the wavelength and the orientation of rolls are about 1 km and 131°, respectively. With the increasing surface heat flux, convective activity intensifies and the rolls become less regular (Figs. 2b,c), although roll vortices are still visible. At midday, the roll spacing becomes large and roll vortices break up. This is in reasonable agreement with the observations that well-defined rolls with a spacing of approximately 1 km and orientated south-southeast existed at 1025 LT, and linear organization broke apart after 1230 LT (Weckwerth et al. 1999). Roll evolution and dissipation from the unforced model run (C1NOF) are very similar (not shown). This shows that relaxing

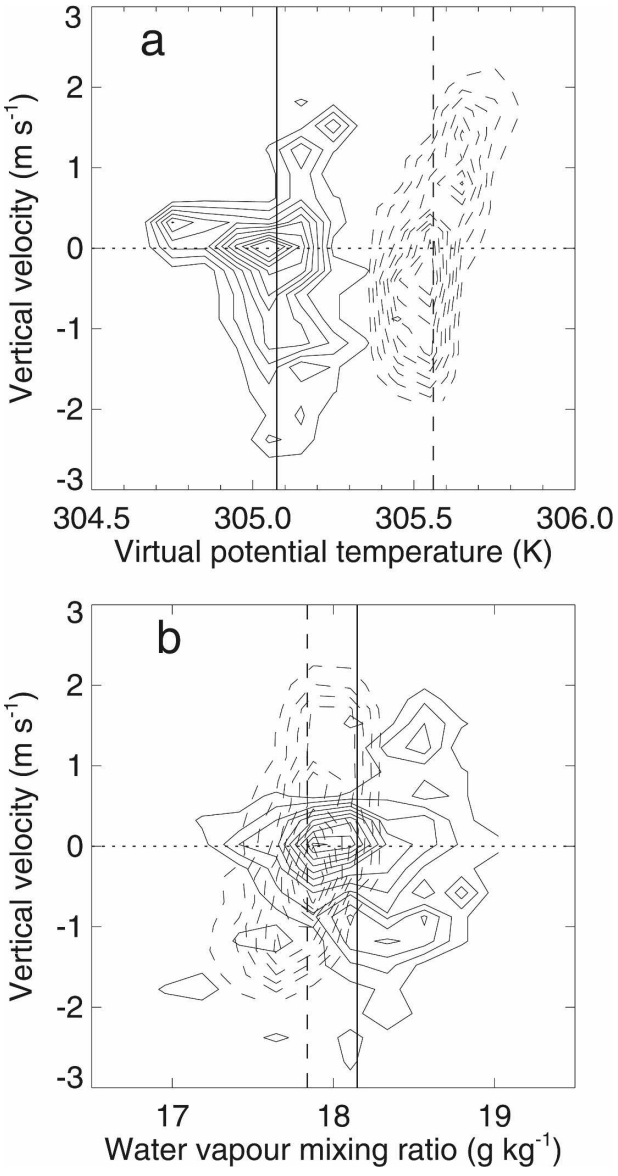

FIG. 3. The joint PDFs of vertical velocities and (a) virtual potential temperatures and (b) water vapor mixing ratios. Solid contours show observations are from 232 m for 5 min around 1100 LT, with the solid line showing the mean values. Dashed contours show model results from 237 m at 1100 LT, with the dashed line showing the mean values. Dotted lines show the mean vertical velocities. Contour intervals are 0.1 in (a) and 0.3 in (b).

the simulation toward the observations had little effect on the convective structures that developed within the modeled boundary layer.

Probability distribution functions (PDFs) allow the comparison of the modeled and observed boundary layer variability. Figure 3 shows the modeled PDFs at 237 m AGL from 1100 LT and observed PDFs at 232 m AGL from 5 min of aircraft data around 1100 LT. On average the simulations are 0.4 K warmer and 0.2 g kg^{-1} drier than the observations, and the modeled and observed vertical velocity fields have similar range (-2 or -3 to 2.5 ms^{-1}). However, there is greater variability in the virtual potential temperatures and Q observed than in those from the model, particularly for vertical velocities close to zero. This may be because mesoscale variations existed in reality (it is more obvious when the segment length for the computation of PDF of the observation increases from 5 to 15 min.) that are not accounted for in the model, which would affect the boundary layer variabilities. The model, which uses periodic lateral boundary conditions and a limited domain, cannot represent such variations. Both the simulations and the observations show higher Q and virtual potential temperatures in updrafts, compared with the downdrafts, although this trend is clearer in the simulations than in the observations.

Other than these differences in the magnitudes of the variability, the dependence of virtual potential temperature and Q on the vertical velocity is well simulated. In particular, in both the model results and observations there are fewer updrafts (which tend to be warm and moist) than downdrafts (which are cooler and drier). This shows that the model is generating realistic boundary layer variability from the convective rolls.

Overall, Figs. 1–3 show that the model produces a realistic development of the boundary layer with time, realistic organization of the convective structures, and realistic boundary layer variability from these convective structures. In the following sections a series of sensitivity experiments are analyzed and the factors that affect modeled roll properties are discussed.

d. Dependence on model resolution

To investigate the effects of model resolution on the results, the control run (C1), which used a horizontal grid spacing of 250 m, was rerun with horizontal grid spacings of 100, 500, and 1000 m. The vertical velocity field from these runs showed that rolls became less organized and less linear when the finer grid spacings were used and finer-scale features were resolved. The 1-km grid spacing did not resolve the rolls at all.

Figure 4 further shows the PDFs of the virtual potential temperature, water vapor mixing ratios, and vertical velocity fields from the runs with different model horizontal resolutions and from 5 min of aircraft data around 1100 LT. Varying the grid spacing has some effect on the mean values in the boundary layer, since although the surface fluxes are identical in all the simulations, changing the model resolution affects the rate of entrainment from the free-troposphere. The distri-

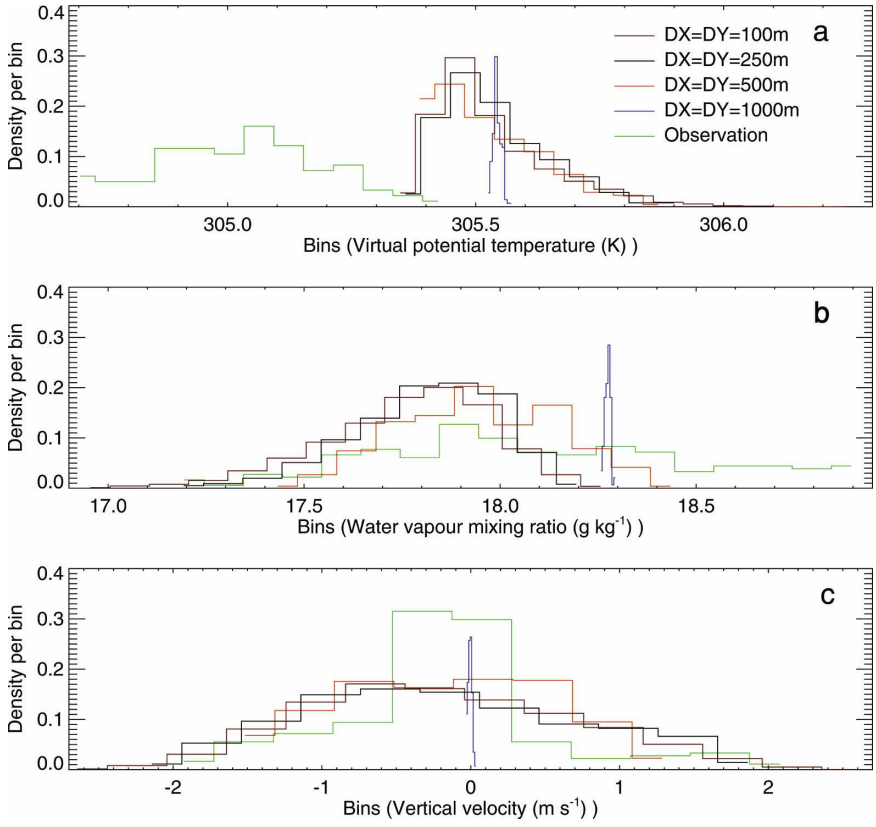

FIG. 4. The PDFs of (a) virtual potential temperature, (b) vapor mixing ratio, and (c) vertical velocity, from runs with horizontal grid spacings of 100, 250, 500, and 1000 m. All are shown for $Z = 237$ m at 1100 LT. Observation is from 232 m for 5 min around 1100 LT.

butions of observed θ_v and Q are more symmetric than the simulated PDFs and there are more vertical velocities observed between -0.5 and 0.3 m s^{-1} than modeled. The 1-km grid spacing, which does not resolve the rolls, gives very narrow PDFs. PDFs from runs using grid spacings of 100 and 250 m are similar, except that the 250-m grid spacing does not resolve the tails as well. The 500-m grid spacing, which coarsely resolves the rolls, gives reasonable PDFs, but there are significant differences in the PDFs from this grid spacing and those from the 100- and 250-m grid spacings. These results agree with Sykes et al. (1988) that convection along the roll direction is less uniform with increased resolution, and Tian and Parker (2003)'s simulated results that a higher horizontal resolution leads to a more fine structure in the rolls. The results also support the use of 250-m grid spacings, which allows a number of sensitivity studies to be performed (sections 3 and 4).

3. Factors controlling the formation and breakup of rolls

Many studies of horizontal convective rolls have described the necessary conditions for the occurrence of rolls using the Monin–Obukhov length (L) and the convective boundary layer height (Z_i). A definition of the Monin–Obukhov length, as given by Stull (1988), is

$$L = \frac{-\overline{\theta}_v(\overline{u'w'_s}^2 + \overline{v'w'_s}^2)^{0.75}}{kg\overline{w'\theta'_{v_s}}}, \quad (1)$$

where the overbar represent the mean values, the subscripts s represent near-surface values, $\overline{\theta}_v$ is the virtual potential temperature, $\overline{u'w'}$ and $\overline{v'w'}$ are the momentum fluxes, k is the von Kármán constant, g is gravitational acceleration, and $\overline{w'\theta'_v}$ is the kinematic buoyancy flux. Studies have observed rolls for $0 \le -Z_i/L \le 4.5$ (Deardorff 1972, using a three-dimensional numerical model), $3 \le -Z_i/L \le 10$ (LeMone 1973, observed), and $-Z_i/L \le 21.0$ (Grossman 1982, observed). In an observational study, Weckwerth et al. (1999) found rolls decaying for $-Z_i/L > 25$ and rolls forming when the surface buoyancy flux increased to a value above 50 W m^{-2}. In this study we examine to what extent the modeled formation and breakup of boundary layer rolls are consistent with these published findings, and also investigate what controls the maximum $-Z_i/L$ for which the modeled rolls occur.

TABLE 1. Surface buoyancy fluxes and geostrophic wind shears for the sensitivity tests. "H" and "G" are the surface buoyancy flux and geostrophic wind shear, respectively, in the control run (C1). CW0 was initialized with wind and geostrophic wind; C0 was initialized with zero wind and geostrophic wind

Condition	C1	C05	C08	C12	C15	CW0	CW05	CW19	CW29	C1NOF	C0
Surface buoyancy flux ($\times H$ W m^{-2})	1.0	0.5	0.8	1.2	1.5	1.0	1.0	1.0	1.0	1.0	1.0
Geostrophic wind shear ($\times G$ s^{-1})	1.0	1.0	1.0	1.0	1.0	0.0	0.5	2.0	3.0	1.0	0.0

Before proceeding further it is necessary to introduce a quantitative measure of roll properties including roll orientation, wavelength, and linearity. A two-dimensional correlation analysis on vertical velocity (w) fields, as described by Weckwerth et al. (1999) and Fankhauser et al. (1995) is used (however, in this study, all the correlation analysis are performed on vertical velocity fields in a Cartesian coordinate system, rather than a polar coordinate system). The vertical velocity (w) field in any x–y slice can be treated as a linear wave in the roll case, so the correlation between w and a cosine function of the form $\cos(2\pi x/\lambda)$, where x is the distance in the cross-roll direction from one grid point to the next one, can be used to determine the orientation and wavelength of rolls. It can also be used to measure the roll organization. In this analysis of the linearity, in order to find the roll orientation, the horizontal axis was first rotated from 0° to 360° with a series of discrete angles to find the maximum correlation coefficient between w and a cosine function in the cross-roll direction, with a specified wavelength in the cross-roll direction. To determine the roll wavelength, this analysis was then repeated for this roll orientation with different wavelengths. The correlation coefficient was used as a measure of linearity, with a threshold of 0.25 used as the criteria for "linear convection" (Weckwerth et al. 1999).

a. Sensitivity to surface heat flux and geostrophic wind shear

To analyze the sensitivity of the modeled rolls to the surface heat flux, four model runs (C05, C08, C12, and C15) were carried out, with 0.5, 0.8, 1.2, and 1.5 times the surface heat flux used in the control run (C1), respectively (Table 1). The vertical velocity fields at 1100 LT (at 237 m AGL) from those four runs (not shown) show that the rolls from runs with reduced surface heat fluxes (C05 and C08) are more linear and regular than those in the control run (Fig. 2c), with smaller vertical velocities, which is consistent with the results of LeMone (1973) and Grossman (1982). Conversely, runs with increased surface heat fluxes (C12 and C15) give less organized rolls than the control run. These model results are consistent with Weckwerth et al. (1997), in that rolls occur within a certain range of surface heat flux.

LeMone (1973) has found that the surface flux controls the intensity of the convection while the CBL vertical wind shear tends to organize convective motions into different forms depending on different shear values (see also Moeng and Sullivan 1994). In our simulations the shear in the boundary layer increases with the geostrophic wind shear applied (as expected from Fig. 1). Four experiments were designed to investigate the effects of wind shear on roll evolution and roll properties. These experiments were configured in the same way as the control run (C1) except that the geostrophic wind shear values are different from that in the C1.

Figure 5 shows the vertical velocity fields (again at 237 m AGL) from four runs in which the geostrophic wind shears are 0 s^{-1} (CW0), 0.0048 s^{-1} (CW05), 0.019 s^{-1} (CW19), and 0.029 s^{-1} (CW29), rather than the value of 0.01 s^{-1} used in the control run C1 (Table 1). All runs are at 1018 LT because well-defined rolls were shown in Fig. 2a. When the geostrophic wind shear is zero (Fig. 5a) the convection is not linear and in a disorganized form. When the geostrophic shear is increased to 0.0048 s^{-1} (Fig. 5b), the convection is more linear than with zero geostrophic wind shear (Fig. 5a), but the rolls are still not very well defined (the rolls are dissipating at this time). If the geostrophic wind shear is increased to 0.019 s^{-1}, clear roll signals appear (Fig. 5c). However, further increasing the geostrophic wind shear to 0.029 s^{-1} has little effect on the rolls linearity (Fig. 5d), but the convection tends to be weaker. It is apparent that, in these simulations, rolls form for geostrophic wind shear values between 0.005 and 0.029 s^{-1} (boundary layer shears between 5×10^{-3} and 6×10^{-3} s^{-1}), when the surface heat flux varies from 40 to 120 W m^{-2}. The results also show that strong wind shear tends to suppress the convection.

b. Linearity of convection

Figure 6 shows the time variation of roll linearity (as defined by the correlation analysis technique described in section 3) in different sensitivity tests (Table 1). The linearity was not analyzed during the first 2 h of the

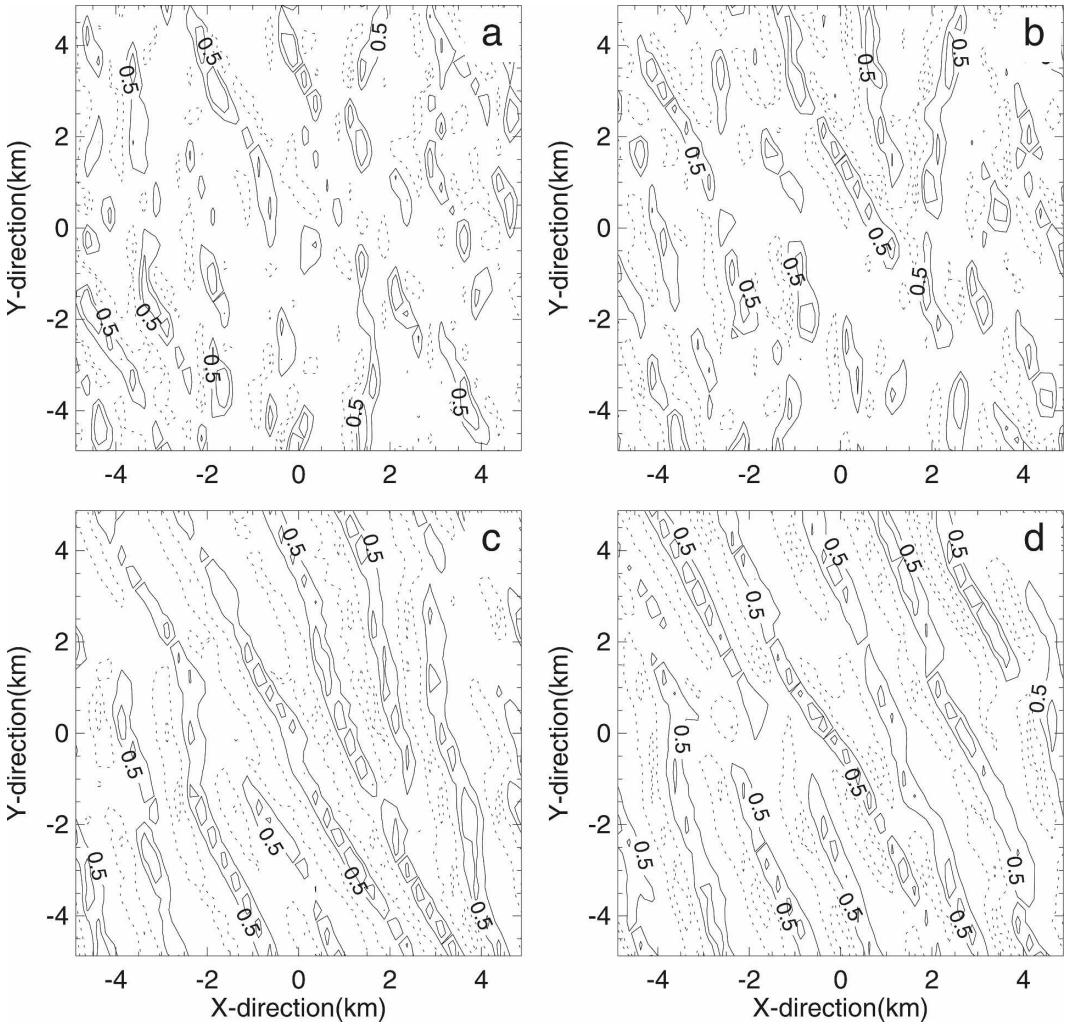

FIG. 5. The instantaneous vertical velocity fields from 237 m AGL at 1018 LT from four runs with (a) 0, (b) 0.5, (c) 2.0, and (d) 3.0 times the geostrophic wind shear of run C1. Contours are at ± 0.5 and ± 1.0 m s^{-1}.

model integration, because some of the simulations were still spinning up (the time series of model kinetic energy suggested that the model was spinning up until 1018 LT for the run C05). Therefore, although in reality linear features were observed from 0940 LT, we calculate the linearity after 1000 LT. The linearity of run C1 (Fig. 6a) increases until 1050 LT, then decreases afterward. For this observed case, Weckwerth et al. (1999) showed a minimum surface heat flux of 90 W m^{-2} for the formation of rolls. In the run C1 the surface heat flux is up to 110 W m^{-2} for roll persistence, and the rolls become less organized after the surface heat flux reaches its maximum. The roll wavelength increased from 1 km at 1018 LT to 1.7 km at 1100 LT, with orientations between 131° at 1018 LT and 146° at 1100 LT. This is in agreement with observations from Weckwerth et al. (1999), which showed rolls with a northwest–southeast orientation, and wavelengths increasing from 1 to 1.5 km between 1025 and 1126 LT. After 1045 LT the development of clouds (see Fig. 12) may contribute to the breaking up of the rolls (LeMone and Pennell 1976).

For a given geostrophic wind shear, small surface heat fluxes correspond to the maxima in the linearity of convection. Rolls appear and begin to dissipate later. When the surface heat fluxes are large (C12 and C15), the convective linearity is lower with an earlier appearance of the maximum values and rolls form and decay earlier compared with those in C05 and C08. This is in agreement with our qualitative analysis of vertical velocity fields from these four runs (not shown). Due to the spinup time required for the model runs, the lower limit of the surface heat flux required for the roll formation cannot be determined. However, the upper

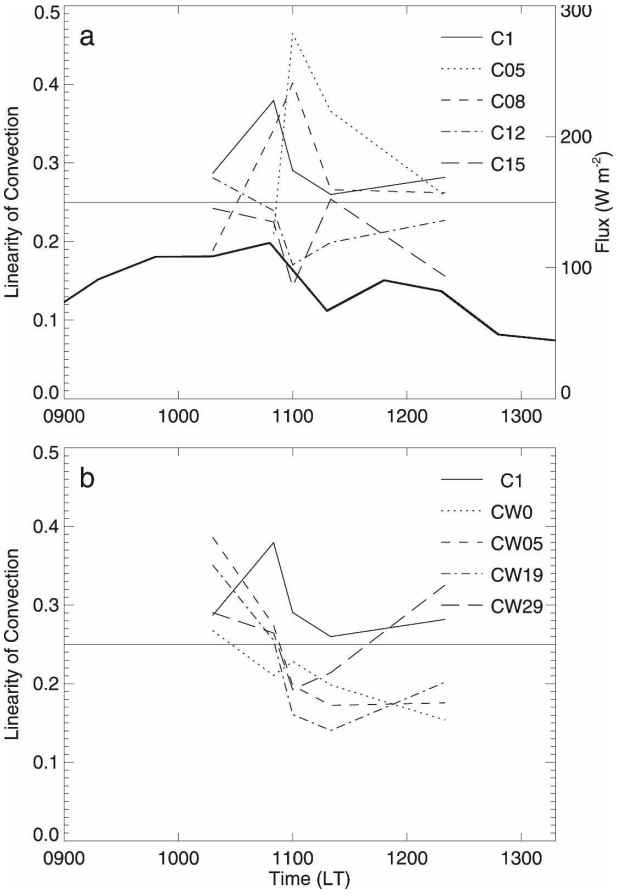

FIG. 6. Evolution of linear convective organization from the control run (C1) and (a) runs with different surface heat flux runs and (b) different geostrophic wind shears (as in Fig. 5). The thick solid line in (a) depict the observed time series of surface buoyancy flux from station Flux-PAM 3.

limit of the surface heat flux for the persistence of rolls is about 110 W m^{-2} in these simulations.

It is evident that the geostrophic wind shear also has a significant effect on the measured linearity of the convection for a given surface heat flux (Fig. 6b). The linearity is very low with zero geostrophic wind shear (CW0) and there is no linear organized convection after 1030 LT in this case (using the threshold of 0.25). This is consistent with a visual analysis of the vertical velocity field shown in Fig. 5a. All cases with a geostrophic wind shear show rolls between 1018 and 1050 LT. Larger geostrophic shears give a smaller maximum in the measured linearity. For CW05, CW19, and CW29, the maximum in linearity appears earlier, suggesting that the rolls are starting to decay earlier. However, it was noted that visual analysis of the vertical velocity field from CW19 at 1120 LT (not shown) showed that rolls did still exist and this highlights the limitation of the linearity method to determine the roll formation and dissipation. However, the results here show that rolls form in the simulations for geostrophic wind shears between 5×10^{-3} and 2.9×10^{-2} s^{-1} (i.e., boundary layer shears between 5×10^{-3} and 6×10^{-3} s^{-1}). This is consistent with Miura (1986)'s study, which also found longitudinal rolls with vertical wind shears between 10^{-3} and 10^{-2} s^{-1}.

c. Dependence on stability parameter $-Z_i/L$

The transition of rolls toward open cells has previously been found to be related to the convective instability variations due to surface heating (e.g., Agee et al. 1973; Weckwerth et al. 1997; Kristovich et al. 1999). Commonly, the parameter $-Z_i/L$ is used to quantify the CBL stability. The Monin–Obukhov length (L) becomes smaller as the surface heat flux becomes larger during the day, while the depth of convection increases as the CBL develops.

Modeled results showed that the value of $-Z_i/L$, when linearity started to decrease, depended both the surface fluxes and the wind shear. Here $Z_i(dU/dz)$ was normalized by the eddy velocity scale, w^*, as given by Stull (1988):

$$w^* = \left(\frac{g}{T_v} Z_i \overline{w'\theta'_{v_s}} \right)^{(1/3)}, \qquad (2)$$

where g is the gravitational acceleration, T_v is the absolute virtual temperature, Z_i is the average depth of the mixed layer, and $\overline{w'\theta'_{v_s}}$ is the kinematic vertical turbulent flux of virtual potential temperature near the surface. Symbols in Fig. 7 show the values of $-Z_i/L$ at the times when rolls began to dissipate (when linearity starts to decrease from a value above 0.25) for runs with different surface heat fluxes and different geostrophic wind shears. (Note that results from additional simulations not listed in Table 1 are included, these included surface heat fluxes and geostrophic winds from 0.2 to 3.0 and 0.2 to 2.0 times the corresponding values used in run C1.) These are shown as a function of the nondimensional term, $(dU/dz)(Z_i/w^*)$ (where dU/dz was calculated by the two levels of winds at 1000- and 100-m altitudes of the model domain). Values at 1018 LT are presented in circles (for wind shears) and big dots (for surface heat fluxes) because the calculation of the linearity was started from 1018 LT due to the model spinups. Rolls begin to dissipate when $5 \leq -Z_i/L \leq 45$, and this threshold depends upon the magnitude of the nondimensional combination of the wind shear, the height of the CBL, and the eddy velocity scale. The critical value of $-Z_i/L$ for rolls to dissipate decreases with increasing wind shear and increases with increasing surface heat flux. The trend shown in Fig. 7 is close to

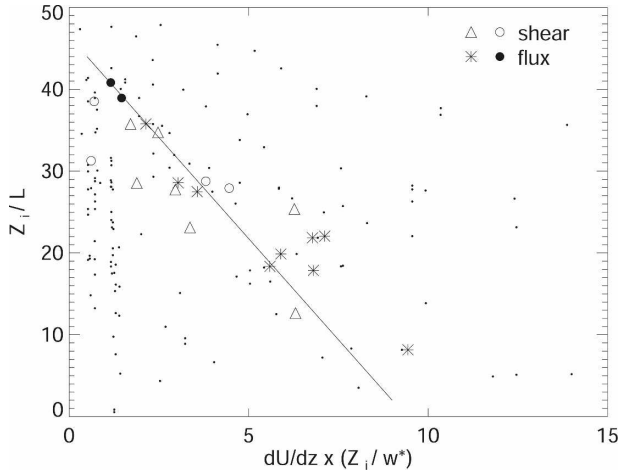

FIG. 7. The modeled variation of $-Z_i/L$ required for the initiation of the dissipation of rolls (i.e., when linearity starts to decrease) from runs with different geostrophic wind shears (triangles and circles) and different surface heat fluxes (stars and big dots). Circles and big dots present the values at 1018 LT. Results from other times during the simulations are shown by small dots.

linear, but the plot shows only a limited range of $(dU/dz)(Z_i/w^*)$ and there is some scatter. Small dots in Fig. 7 show results at other times during the simulations. These show that the results effectively populate the parameter space and that the linear trend shown for the onset of breaking up (shown by the symbols) is not due to a linear relationship between the ordinate and abscissa variables in Fig. 7 at all times.

4. The effect of rolls on boundary layer variability and the deepening of the moist convection

It is known that interaction between convergence zones and convective rolls can play an important part in the initiation of deep convection, and in the absence of other significant sources of convergence, deep convection can be initiated from boundary layer rolls. In this section the control case (C1) is compared with a nonroll case (C0). This nonroll case is initialized with no wind, no geostrophic wind shear, and no wind forcing. The effects of the rolls on boundary layer variability and the implications of this variability on CIN (and so the deepening of the moist convection) are examined. Finally the modeled development of moist convection in C1 and C0 is compared.

a. Rolls and boundary layer variability

Figure 8 shows the PDFs of the equivalent potential temperature, water vapor mixing ratio, and vertical velocities at the different CBL heights (i.e., 0.3, 0.7 and 1.0 Z_i) from the control run (C1) and the nonroll run (C0) at 1100 LT, as clouds had just started to form (see Fig. 12). To compare the "tails" of the PDFs, a logarithmic scale is used for the y axis. In both the roll and the nonroll simulations updrafts tended to be warm and moist (i.e., high θ_e), and downdrafts cool and dry (e.g., Fig. 3). Overall, the distributions of water vapor mixing ratios show more significant variations with respect to their means (1.0–2.2 g kg^{-1}) than those of virtual potential temperature (not shown, 0.3 − 0.5 K). This is because moisture fields have greater vertical gradient than the virtual potential temperature fields (e.g., Mahrt 1976; Weckwerth 1996). From 0.3 to 0.7 Z_i the distribution of Q is negatively skewed, with the peak of the distribution close to its right-hand side. At 1.0 Z_i the Q distribution becomes much flatter because of the entrainment of the warm and dry air from above the CBL. The skewness decreases with increasing altitude, which is agreement with Couvreux et al. (2005). Similarly, the PDFs of equivalent potential temperature (Figs. 8b,e,h) are negatively skewed at 0.7 Z_i, flatter at 1.0 Z_i and more symmetric at 0.3 Z_i.

The distribution of vertical velocity (Figs. 8c,f,i) is positively skewed within the CBL, which is consistent with other LEM studies of surface heating–driven PBL (Moeng and Wyngaard 1988). Moeng and Rotunno (1990) found that this was because there are fewer but stronger updrafts with the subsidence between them at the top of the PBL than at lower levels. The roll convection leads to more symmetric PDFs of vertical velocity than the nonroll convection; the nonroll convection has fewer, but stronger, updrafts and more, but weaker, downdrafts. This nonroll convection is therefore similar to that described by Couvreux et al. (2005), with narrow plumes of ascending air with broader regions of weak descent.

Low in the CBL (0.3 Z_i) the differences in updrafts between the roll and nonroll cases are small, but there are more strong downdrafts in the roll convection than in the nonroll convection. These downdrafts tend to be moister. Higher in the CBL (0.7 Z_i), the differences in updrafts between the roll case and the nonroll case become more significant. In the nonroll case, there are stronger updrafts than in the roll case, and these strong updrafts are moister and have higher equivalent potential temperatures. The results of Figs. 8 and 9 show the occurrence of stronger buoyant moist updrafts without rolls before 1130 LT. The differences in downdrafts are similar to those in the lower CBL, with roll convection giving more strong downdrafts. At the top of the CBL (1.0 Z_i), the updrafts in the nonroll convection again tend to be stronger, while the downdrafts in the roll convection become drier than those of the nonroll con-

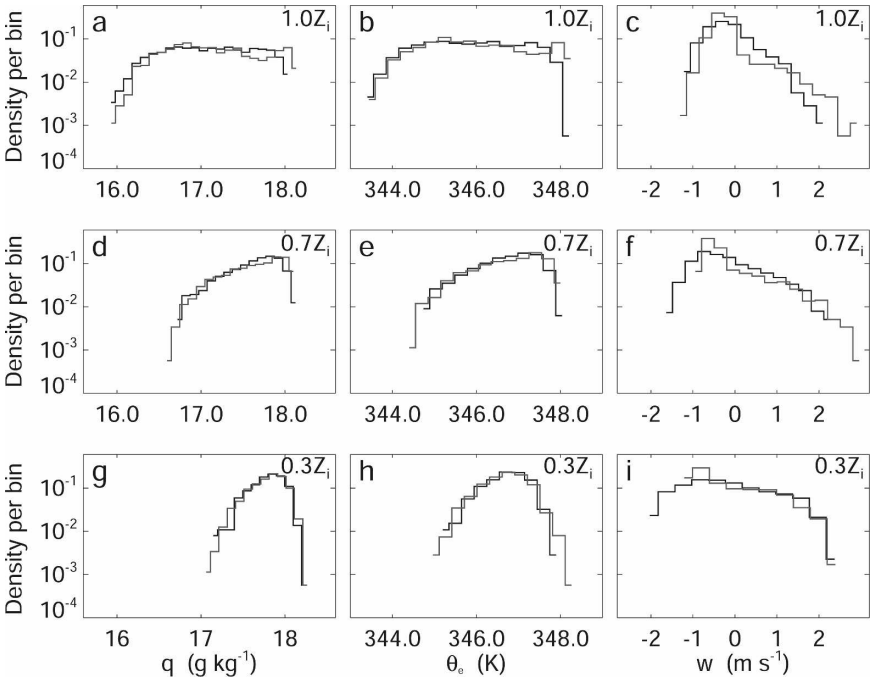

FIG. 8. The PDFs of (a), (d), (g) mixing ratio; (b), (e), (h) equivalent potential temperature; and (c), (f), (i) vertical velocity from the control run C1 (black lines) and run C0 (gray lines). All are at 1100 LT and from $Z = 0.3Z_i$ in (g), (h), (i); $Z = 0.7Z_i$ in (d), (e), (f); and $Z = 1.0Z_i$ in (a), (b), (c).

vection (Figs. 8a–c). This nonroll convection again agrees with the model described by Couvreux et al. (2005), with only the strongest updraft plumes persisting to the top of the CBL. In summary, the differences in the CBL variabilities between the roll and nonroll case are most significant at the top of the CBL, with stronger moist updrafts (with high values of θ_e) existing in the nonroll convection.

After 1130 LT, when clouds had almost reached their maximum height (section 4b) the maximum of vertical velocities were larger for the roll case, and the maximum of equivalent potential temperatures were larger for the nonroll convection (Fig. 9). To check whether these differences were from the differences in the model spinups between C1 (rolls) and C0 (nonrolls), C1 was rerun forcing the mean horizontal wind to be zero after the spinup period (i.e., after 1000 LT). This gave a nonroll case with a spinup period identical to the roll case (C1) after an approximately 15-min adjustment. This gave very similar variations in $\theta_{e\max}$ and $w_{\max}$ to the standard nonroll run, showing that the differences presented in Fig. 9 are not from different model spinups.

Figure 10 shows how updrafts lift the top of the CBL and correspond to regions of low CIN, while downdrafts correspond to larger values of CIN. To compute CIN, the instantaneous virtual potential temperature field from the model simulation is taken as the environment profile, θ_{ve}, air parcels, which are lifted from the surface level are considered and a pseudoadiabatic process is assumed in calculating the parcel virtual potential temperature θ_{vp}. In the roll case, the convection is more regularly organized, with more strong downdrafts. Updrafts give lower CIN since they lift the lid at the top of the CBL and since the source air tends to be warmer and moister than average.

To evaluate the relative contributions from the variations in the source air and the variations in the profile, the CIN was calculated using three different methods (Fig. 11). Method 1 calculated CIN for each column within the model, with the source air coming from the lowest model level. Method 2 used the mean model profile, but with source air parcels from the lowest model level, and method 3 used mean values of temperature and Q from the lowest model level for the source air. Therefore, method 1 allowed both variations in the source air and the profile, method 2 allowed only variations in the source air to contribute, and method 3 allowed only the variations in the profile to affect CIN.

Rolls give fewer strong moist updrafts and more strong downdrafts (Fig. 8) and Fig. 11a shows that this leads to more high CIN values (>11.5 J kg^{-1}) with rolls,

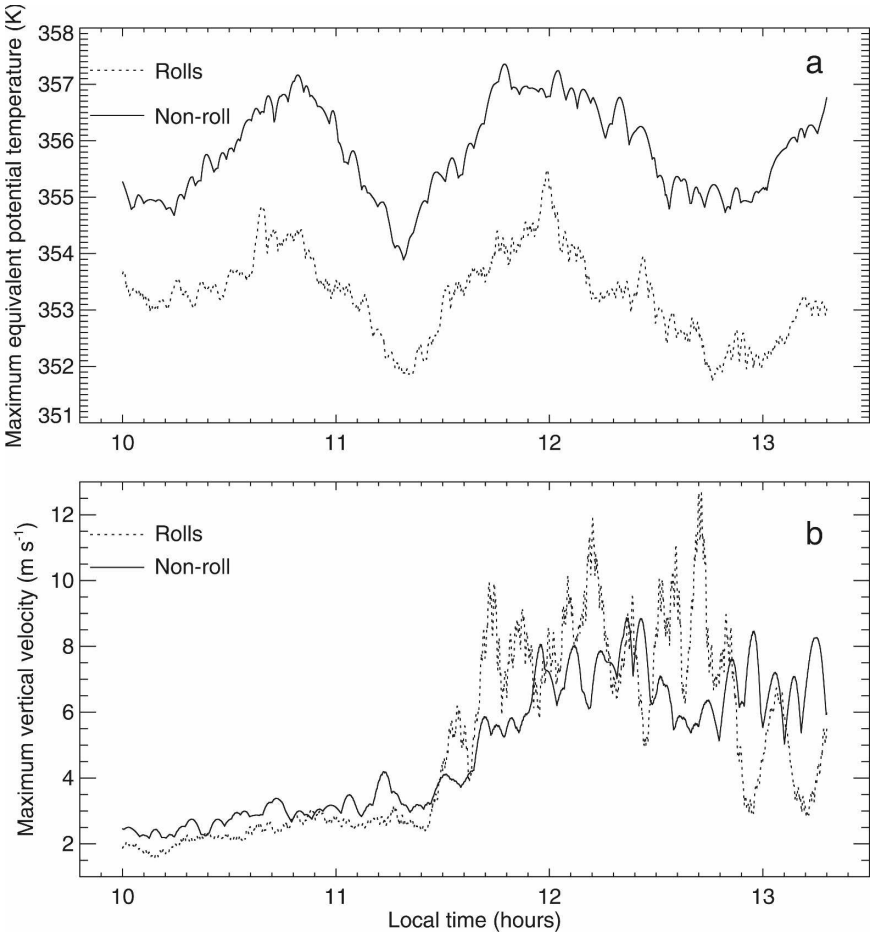

FIG. 9. Time variations of the modeled (a) maximum of equivalent potential temperature and (b) maximum of vertical velocity from the 3D model field.

and more very low CIN values (<2 J kg^{-1}) without rolls. Figures 11b,c show that the variability in the source air, caused by the boundary layer convection, dominates the modeled variations in CIN for both the roll and nonroll cases. The variability in the model profile, with the raised lid at the top of the CBL in convective updrafts, has a significant, but smaller, contribution. This lifting has larger effects for the nonroll case than the roll case (Fig. 11c), and the variability in the source air has larger effects in the roll case (Fig. 11b).

b. The deepening of the convection

Section 4a shows the effects of rolls on BL variability and CIN. In this section the modeled development of the deeper moist convection is investigated. As already noted, deep moist convection was not observed on this day, but there was sufficient CAPE to allow a transition from the boundary layer cumulus in the LEM to moist convection of a moderate depth, with cloud tops at approximately 2.7 km. Clouds developed from a cloud base approximately 900 m and the cloud fraction reached approximately 15%.

Figure 12 shows that the modeled clouds deepened approximately 15 min earlier in the nonroll case (ensembles of simulations were used to ensure that results were robust to changing the random numbers used to initialize the runs). However, in the roll case clouds deepen slightly more rapidly than in the nonroll case, so the cloud tops reach 2.7 km at approximately the same time. To allow deeper convection to form, C1 and C0 were rerun with the CAPE increased. This was achieved by cooling the initial potential temperature profile above the height where the CIN vanished by 2 K, and allowed the cloud tops to reach 4 km. Again the nonroll case gave deep moist convection earlier than the roll case (Fig. 12 "cold"). The results were also robust to removing the relaxation to the observed profiles applied over the first three hours of the simulations. These results, with earlier deep moist convection

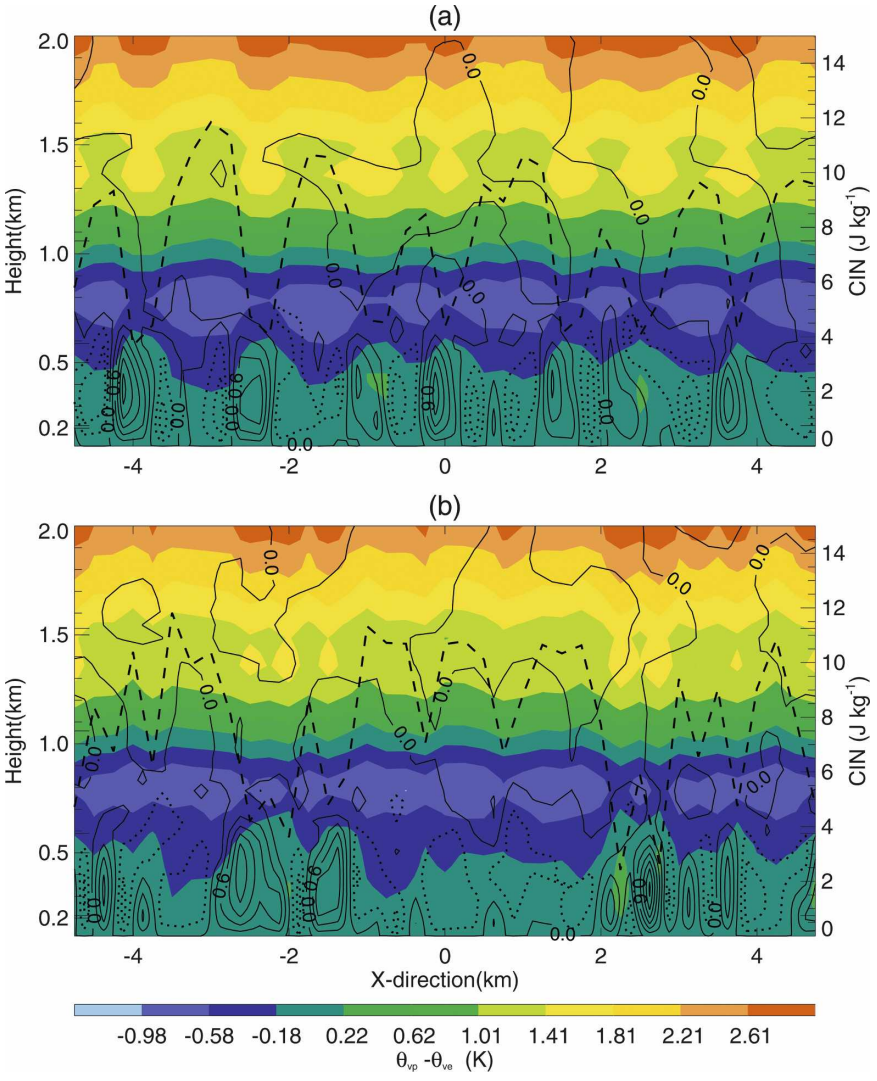

FIG. 10. Instantaneous x–z cross sections of the CIN, buoyancy, and vertical velocity at 1018 LT for (a) the roll case and (b) the nonroll case. The dashed lines show the CIN; the solid and dotted contours show the updrafts and downdrafts with 0.3 m s^{-1} contour intervals; buoyancy ($\theta_{vp} - \theta_{ve}$) is shaded.

without rolls, are consistent with section 4a, which is consistent with nonroll convection giving stronger updrafts with lower values of CIN. After 1130 LT, the rolls gave stronger maximum updrafts (but still lower maximum equivalent potential temperatures), but at this time the clouds had almost reached their maximum height (Figs. 9 and 12). This suggests that, for a different case with more CAPE, roll convection may allow a more rapid growth of convection after the initial stage in the cloud development.

5. Conclusions

Convective rolls, and the thermodynamic variability associated with rolls, have been studied using three-dimensional LEM simulations. Although the precise time development of the modeled boundary layer differs slightly from that observed (after 3 h the modeled boundary layer is approximately 0.4 K warmer and 0.2 g kg^{-1} drier than observed), the modeled temperature, humidity, and vertical velocity fluctuations are in good agreement with those observed. Both the simulations and the observations show that the roll convection is characterized by narrow warm and moist updrafts and broader drier downdrafts. Increasing the model horizontal grid spacings from 100 to 500 m gave very similar bulk properties of the CBL, but smaller tails to the PDFs of virtual potential temperature, Q, and vertical velocities. Increasing the grid spacing to 1 km gave

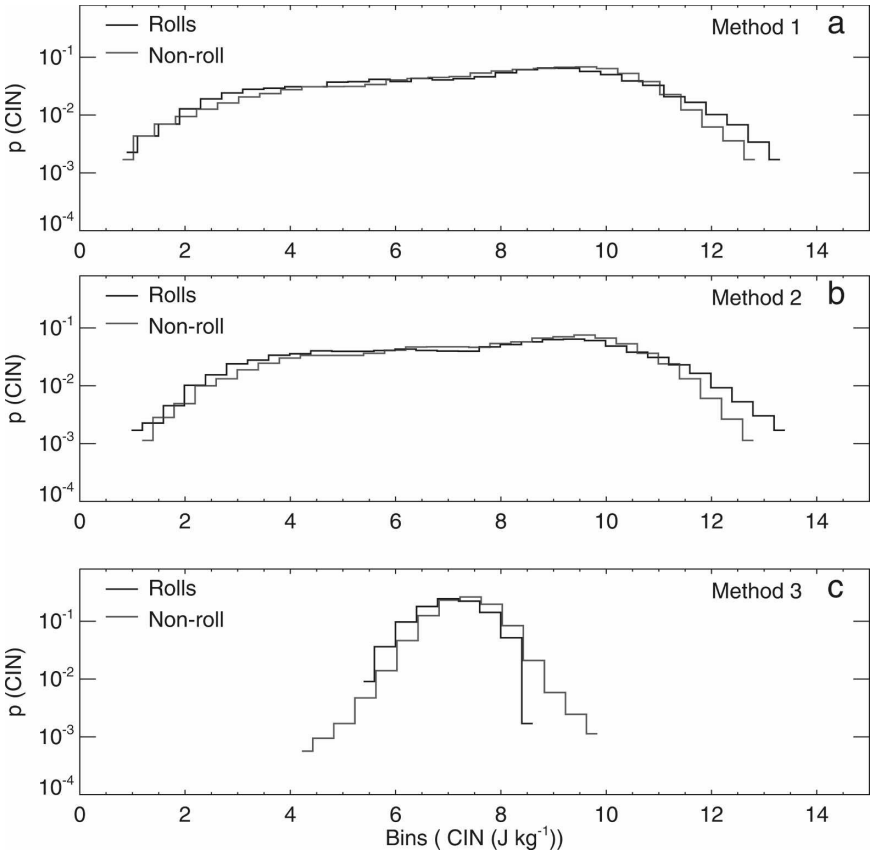

FIG. 11. PDFs of CIN from the roll case (black lines) and the nonroll case (gray lines) at 1018 LT, using three methods: (a) method 1 (standard calculation), (b) method 2 (using the mean profile), and (c) method 3 (using the mean source air).

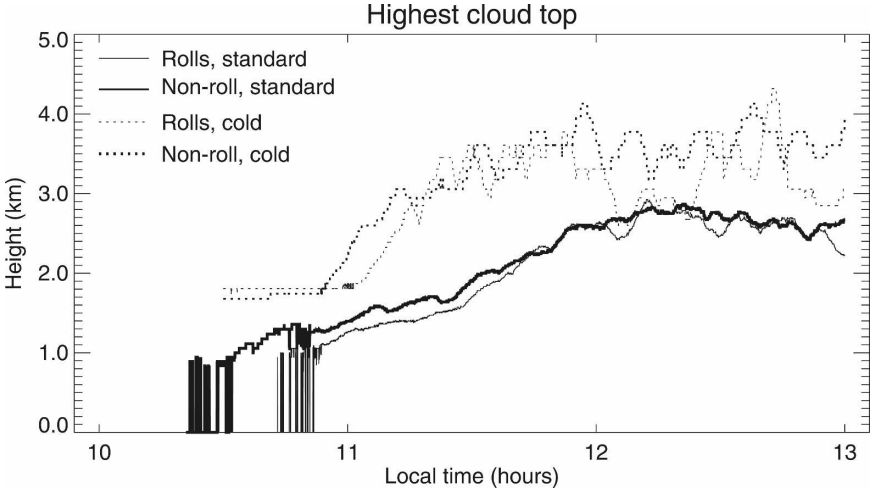

FIG. 12. Time variations of the cloud top for the rolls case (thin lines, C1) and nonroll case (thick lines, C0). Mean values from the 8-member ensembles are shown, with each member of the ensemble using different random numbers to initialize the run. Results from the cold profile runs with increased CAPE are also shown (single runs not ensembles).

much narrower PDFs than observed, since this grid spacing did not resolve the convective rolls.

In accordance with the previous findings, rolls form with moderate surface heat fluxes and some minimal wind shear, and the model results show that the roll formation is indeed sensitive to the magnitudes of the surface heat flux and the geostrophic wind shear. The results show that rolls start to decay when the value of $-Z_i/L$ exceeds a value between 5 and 45, which is dependent upon a nondimensionalized combination of the low-level wind shear, the height of the CBL, and the eddy velocity scale [i.e., $(dU/dz)(Z_i/w^*)$]. For larger heat fluxes, rolls dissipate with larger $-Z_i/L$, due to the smaller values L in such cases. For larger geostrophic wind shears, rolls decay with smaller values of $-Z_i/L$ because of the larger values of L. For this SCMS case the upper limit on the surface heat flux for the persistence of rolls in the model is approximately 110 W m^{-2}. The model results also show that rolls form for geostrophic wind shears between 0.005 and 0.029 s^{-1} (i.e., boundary layer shears between 5×10^{-3} s^{-1} and 6×10^{-3} s^{-1}), which is consistent with previous studies.

To investigate the significance of boundary layer rolls for the initiation of deep convection, boundary layer variability was compared for roll and nonroll simulations, which were identical except for the wind and the wind shear used. In both cases the variability in the temperature and humidity of the source air dominated the contribution made by the variability of the profile to the variability in CIN. Therefore, in this case at least, it is the variability in boundary layer thermodynamic properties, rather than the lifting of the CBL top by boundary layer convection that is most significant for the reduction of CIN. This highlights the importance of accurately parameterizing such variability in NWP models, which do not resolve this boundary layer convection.

The distribution of vertical velocity is positively skewed for both roll and nonroll cases. However, PDFs of vertical winds were more symmetrical in the roll case, while the nonroll case gave stronger moist updrafts, with larger areas of weak downdrafts. These differences became more significant at the higher altitudes within the CBL. As a result of these warmer moister updrafts, the nonroll convection had the lowest minimum values of CIN, which allowed cloud-top heights to increase approximately 15 min earlier than in the roll case. It should be noted that in this case limited CAPE meant that both roll and nonroll cases gave similar maximum cloud-top heights of only approximately 2700 m (and 4000 m in a run with a modified profile). Therefore, for cases with deeper convection, other processes may dominate, such as the differences in entrainment into clouds initiated from rolls and from nonlinearly organized convection. These processes are, however, outside the scope of this particular study.

Acknowledgments. This work has been supported by National Basic Research Program of China (2006CB400501). The surface flux measurements and sounding data were obtained from NCAR/EOL, which is supported by the U.S. National Science Foundation. The UWKA measurements were obtained from the University of Wyoming. John Marsham was supported by NERC Grants NER/O/S/2002/00971 and NE/E006124/1. Q. Huang also thanks the School of Earth and Environment, University of Leeds, for computer support during this study. We would also like to thank all the reviewers for their comments on the paper, which resulted in significant improvements, both in clarity and content.

REFERENCES

Agee, E. M., T. S. Chen, and K. E. Doswell, 1973: A review of mesoscale cellular convection. *Bull. Amer. Meteor. Soc.,* **54,** 1004–1012.

Atkins, N. T., R. M. Wakimoto, and C. L. Ziegler, 1998: Observations of finescale structure of a dryline during VORTEX. *Mon. Wea. Rev.,* **126,** 525–550.

Bennett, L. J., K. A. Browning, A. M. Blyth, D. J. Parker, and P. A. Clark, 2006: A review of the initiation of precipitating convection in the United Kingdom. *Quart. J. Roy. Meteor. Soc.,* **132,** 1001–1020.

Browning, K., and Coauthors, 2007: The Convective Storm Initiation Project. *Bull. Amer. Meteor. Soc.,* **88,** 1939–1955.

Chlond, A., 1987: A numerical study of horizontal roll vortices in neutral and unstable atmospheric boundary layers. *Beitr. Phys. Atmos.,* **60,** 144–169.

Couvreux, F., F. Guichard, J. L. Redelsperger, C. Kiemle, and V. Masson, 2005: Water-vapour variability within a convective boundary-layer assessed by large-eddy simulations and IHOP_2002 observations. *Quart. J. Roy. Meteor. Soc.,* **131,** 2665–2693.

Crook, N. A., 1996: Sensitivity of moist convection forced by boundary layer processes to low-level thermal dynamic fields. *Mon. Wea. Rev.,* **124,** 1767–1785.

——, M. W. Moncrieff, and T. L. Clark, 1991: The Denver cyclone. Part II: Interaction with the convective boundary layer. *J. Atmos. Sci.,* **48,** 2109–2126.

Cuijpers, J. W. M., and P. G. Duynkerke, 1993: Large eddy simulation of trade wind cumulus clouds. *J. Atmos. Sci.,* **50,** 3894–3908.

Deardorff, J. W., 1972: Numerical investigation of neutral and unstable planetary boundary layers. *J. Atmos. Sci.,* **29,** 91–115.

Etling, D., and R. A. Brown, 1993: Roll vortices in the planetary boundary layer: A review. *Bound.-Layer Meteor.,* **65,** 215–248.

Fankhauser, J. C., N. A. Crook, J. Tuttle, L. J. Miller, and C. G. Wade, 1995: Initiation of deep convection along boundary layer convergence lines in a semitropical environment. *Mon. Wea. Rev.,* **123,** 291–313.

Glendening, J. W., 1996: Linear eddy features under strong shear conditions. *J. Atmos. Sci.,* **53,** 3430–3449.

Gray, M. E. B., and J. Petch, 2001: Version 2.3 of the Met. Office large eddy model. Part II: Scientific documentation. Turbulence and Diffusion, Note 276, Met Office, Exeter, United Kingdom.

Grossman, R. L., 1982: An analysis of vertical velocity spectra obtained in the BOMEX fair-weather, trade-wind boundary layer. *Bound.-Layer Meteor.,* **23,** 323–357.

Kristovich, D. A., R. N. F. Laird, M. R. Hjelmfelt, R. G. Derickson, and K. A. Cooper, 1999: Transitions in boundary layer meso-convective structures: An observational case study. *Mon. Wea. Rev.,* **127,** 2895–2909.

LeMone, M. A., 1973: The structure and dynamics of horizontal roll vortices in the planetary boundary layer. *J. Atmos. Sci.,* **30,** 1077–1091.

——, and W. T. Pennell, 1976: The relationship of trade wind cumulus distribution to subcloud layer fluxes and structure. *Mon. Wea. Rev.,* **104,** 524–539.

Mahrt, L., 1976: Mixed layer moisture structure. *Mon. Wea. Rev.,* **104,** 1403–1407.

Marsham, J. H., J. S. E. Dobbie, and R. J. Hogan, 2006: Evaluation of a large-eddy model simulation of a mixed-phase altocumulus cloud using microwave radiometer, lidar and Doppler radar data. *Quart. J. Roy. Meteor. Soc.,* **132,** 1693–1715.

Marson, P. J., 1985: A numerical study of cloud streets in the planetary boundary layer. *Bound.-Layer Meteor.,* **32,** 281–304.

Mason, P. J., and R. I. Sykes, 1982: A two-dimensional numerical study of horizontal roll vortices in an inversion capped planetary boundary layer. *Quart. J. Roy. Meteor. Soc.,* **108,** 801–823.

——, and D. I. Thomson, 1987: Large-eddy simulation of the neutral-static-stability planetary boundary layer. *Quart. J. Roy. Meteor. Soc.,* **113,** 413–443.

Miura, Y., 1986: Aspect ratio of longitudinal rolls and convection cells observed during cold air outbreaks. *J. Atmos. Sci.,* **43,** 26–39.

Moeng, C.-H., and J. C. Wyngaard, 1988: Spectral analysis of large-eddy simulations of convective boundary layer. *J. Atmos. Sci.,* **45,** 3575–3587.

——, and R. Rotunno, 1990: Vertical-velocity skewness in the buoyancy-driven boundary layer. *J. Atmos. Sci.,* **47,** 1149–1162.

——, and P. P. Sullivan, 1994: A comparison of shear and buoyancy driven planetary-boundary-layer flows. *J. Atmos. Sci.,* **51,** 999–1022.

Raasch, S., 1990: Two numerical studies of horizontal roll vortices in near-neutral inversion capped planetary boundary layer. *Beitr. Phys. Atmos.,* **63,** 205–227.

Stull, R. B., 1988: *An Introduction to Boundary Layer Meteorology.* Kluwer Academic, 666 pp.

Sykes, R. I., W. S. Lewellen, and D. S. Henn, 1988: A numerical study of the development of cloud-street spacing. *J. Atmos. Sci.,* **45,** 2556–2570.

——, ——, and ——, 1990: Numerical simulation of the boundary layer eddy structure during the cold-air outbreak of GALE IOP-2. *Mon. Wea. Rev.,* **118,** 363–374.

Tian, W., and D. J. Parker, 2003: Observations and numerical simulation of atmospheric cellular convection over mesoscale topography. *Mon. Wea. Rev.,* **131,** 222–235.

Weckwerth, T. M., 1996: Thermodynamic variability within the convective boundary layer due to horizontal convective rolls. *Mon. Wea. Rev.,* **124,** 770–784.

——, 2000: The effect of small-scale moisture variability on thunderstorm initiation. *Mon. Wea. Rev.,* **128,** 4017–4030.

——, J. W. Wilson, R. M. Wakimoto, and N. A. Crook, 1997: Horizontal convective rolls: Determing the environmental conditions supporting their existence and characteristics. *Mon. Wea. Rev.,* **125,** 505–526.

——, T. W. Horst, and J. W. Wilson, 1999: An observational study of the evolution of horizontal convective rolls. *Mon. Wea. Rev.,* **127,** 2160–2179.

Wilson, J. W., and W. E. Schreiber, 1986: Initiation of a convective storm at radar-observed boundary convergence lines. *Mon. Wea. Rev.,* **114,** 2516–2536.

——, and R. D. Roberts, 2006: Summary of convective storm initiation and evolution during IHOP: Observational and modeling perspective. *Mon. Wea. Rev.,* **134,** 23–47.

——, G. B. Foote, N. A. Crook, J. C. Fankhauser, C. G. Wade, J. D. Tuttle, C. K. Mueller, and S. K. Krueger, 1992: The role of boundary-layer convergence zones and horizontal rolls in the initiation of thunderstorms: A case study. *Mon. Wea. Rev.,* **120,** 149–171.

Wulfmeyer, V., 1999: Investigation of humidity skewness and variance profiles in the convective bounday layer and comparison of the latter with large eddy simulation results. *J. Atmos. Sci.,* **56,** 1077–1087.

Xue, M., and W. J. Martin, 2006: A high-resolution modeling study of the 24 May 2002 dryline case during IHOP. Part II: Horizontal convective rolls and convective initiation. *Mon. Wea. Rev.,* **134,** 172–191.